Unravelling heparin's enhancement of amyloid aggregation in a model peptide system

Suhas Gotla[a], Anushka Poddar[a], Ilana Borison[a], and Silvina Matysiak[a,*]

[a]Fischell Department of Bioengineering, University of Maryland, College Park, MD 20742, United States of America
[*]Corresponding author. matysiak@umd.edu

Supplementary Information: Heparin model parameterization and Supplementary figures, tables and movie captions

1 Heparin model parameterization

1.1 Atomistic reference simulations for bonded interaction tuning

The PDB structure 3IRL, solved by solution scattering,[1] was used as the initial structure for our atomistic simulations. This heparin fragment consists of eighteen repeats of the most common heparin disaccharide, [α-L-iduronic acid-(1$\rightarrow$4)-α-D-glucosamine-(2,6)-disulfate], abbreviated here as (IDO-GDS). Forcefield files, based on CHARMM36,[2] for this heparin fragment were generated using the Glycan Reader & Modeler module[3] of the web-based tool, CHARMM-GUI.[4] The heparin fragment was placed in a 13.4 nm cubic box with, roughly, 75000 TIP3P water particles. To balance the heparin fragment's charge (each monosaccharide contained two monovalent anionic groups), 72 potassium counterions were introduced. All necessary files for simulation were generated for GROMACS using the Input Generator module.[5,6]

The solvated structure was equilibrated with 5000 steps of steepest-descent energy minimization, followed by 125000 steps of NVT simulation at 0.001 ps time-steps with harmonic position restraints on solute particles. For the production run, bonds involving hydrogen were replaced by LINCS constraints[7] and time-steps were increased to 0.002 ps. 200 ns of NPT simulation were performed using an isotropic Parrinello-Rahman barostat fixed at a pressure of 1 bar, with a time constant and compressibility of 5 ps and 4.5e-5 bar^{-1}, respectively.[8] Temperature for the NPT production run, as well as the NVT equilibration step, was fixed with a Nose-Hoover thermostat at 303.15 K (i.e., 30^o C), with a time constant of 1 ps, applied separately to the solvent and solute particles.[9] Newton's equations of motion were integrated using a leap-frog algorithm. Pair lists for non-bonded interaction calculations were generated using a Verlet scheme, with a 1.2 nm cut-off updated every 20 time-steps. Short-range van der Waals forces were smoothly switched off from 1.0 to 1.2 nm. Short-range electrostatics were computed until a plain cut-off of 1.2 nm. Long-range electrostatics were computed using the Particle-Mesh Ewald scheme.[10]

1.2 CG Heparin Model Construction

Non-bonded interactions Our CG model for heparin consists of a sequence of IDO-GDS disaccharides. The atoms were grouped into CG beads such that their partial charges would sum up to either 0 e or -1 e. In effect, the structure of each CG monosaccharide is represented by four main beads: Anionic beads B2 and B6 representing sulfate and carboxylate groups on the 2' and 6' carbon positions of the pyranose ring, and polar beads BG and B3 representing the glycosidic backbone, and 3' carbon group atoms with net-zero charge.

The van der Waals diameters (σ in the Lennard-Jones potential) of BG and B2 of IDO and GDS, and B6 of GDS were set at the standard MARTINI diameter of 0.47 nm. On the other hand, the van der Waals diameters of B6 of IDO, and B3 of GDS and IDO were scaled to 75% and 68% of the standard diameter to account for the smaller number of atoms mapping to the beads. These scaling factors were borrowed from the MARTINI models for nucleic acids,[11] where the so-called "tiny" (scaled by 68%) beads were introduced alongside the "small" (scaled by 75%) and standard beads. The Lennard-Jones interaction levels (well depth, ϵ, of the Lennard-Jones potential) for BG, B2 and B3 beads

were set at MARTINI levels P1, Qa and TN0, respectively. B6 beads of GDS and IDO were set at MARTINI levels Qa and SQa, respectively.

As in the MARTINI polarizable water model[12] and the ProMPT forcefiled for proteins[13] the neutral polar beads, BG and B2, were modelled with internal Drude-like oscillators to emulate the inherent dipole moments of their corresponding atoms. The partial charges of the dummy particles, and parameters of their related bonded interactions with the central beads, were tuned such that the CG dipole moment distributions matched their atomistic counterparts (Fig. S1).

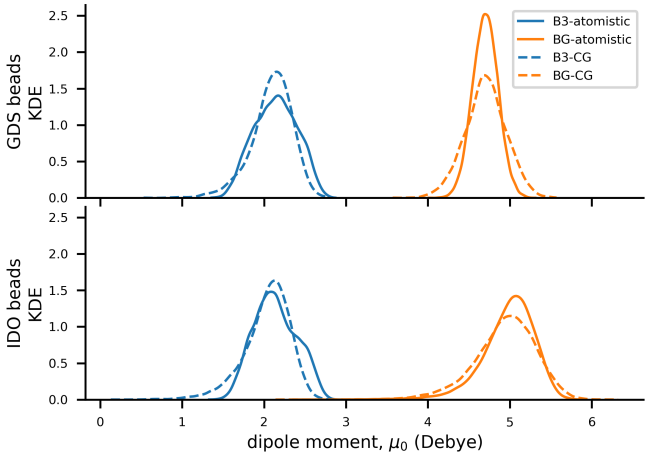

Figure S1: Distributions of dipole moments (magnitude of the dipole vector, $\vec{p} = \sum_{i=1}^{N} q_i \cdot \vec{r_i}$, where q_i and r_i are the charge and position of a particle i, respectively) of CG polarized beads BG and B3 (dashed lines), and their corresponding atomistic reference atoms (solid lines).

To avoid over-polarization in addition to the dummy charge, a small hard-core repulsive potential was used (Lennard-Jones coefficient, $4\epsilon\sigma^{12} = 4.5387e-10\ kJ\ nm^{12}mol^{-1}$). To correct for the additional electrostatic interactions in polarized beads through their dummy charges, all polarized bead-polarized bead interactions (e.g., BG-BG) were scaled down by $0.58kJ/mol$, and all charged bead-polarized interactions (e.g. BG-B6) were scaled down by $0.28kJ/mol$. To distinguish the original MARTINI beads from their polarized counterparts, we have renamed bead types P1 and TN0 as PP1 and PTN0, respectively.

Bead names, types, and charges for the heparin residues IDO and GDS (Figure 1) are summarized in Table S1. Furthermore, Table S2 details the Lennard-Jones self-and cross-interactions between all the bead types used to represent heparin, the $A\beta_{16-22}$ peptides, and solvent particles.

Table S1: Bead types and charges for CG heparin residues, IDO and GDS

Residue	Bead name	Bead type	Charge (e)
IDO, α-L-iduronic acid	BG	PP1	0
	BGm	D2	0.38
	BGp	D2	-0.38
	B2	Qa	-1
	B3	PTN0	0
	B3m	D2	0.24
	B3p	D2	-0.24
	B6	SQa	-1
GDS, α-D-glucosamine-(2,6)-disulfate	BG	PP1	0
	BGm	D2	0.35
	BGp	D2	-0.35
	B2	Qa	-1
	B3	PTN0	0
	B3m	D2	0.24
	B3p	D2	-0.24
	B6	Qa	-1

Table S2: parameters for Lennard-Jones interactions between various bead types ($V_{LJ}(r) = 4\epsilon\left[(\frac{\sigma}{r})^{12} - (\frac{\sigma}{r})^{6}\right]$)

Lennard-Jones well depth, ϵ (kJ mol^{-1})

	PP1	PP5	PTN0	Qa	SQa	Qd	POL	C3	C1	AR
PP1	3.9	5.0	3.4	5.3	5.3	5.3	3.7	3.5	2.7	2.7
PP5	5.0	5.0	2.9	5.3	5.3	5.3	4.7	2.7	2.0	2.0
PTN0	3.4	2.9	2.0	3.7	2.7	3.7	2.7	3.5	2.7	2.0
Qa	5.3	5.3	3.7	3.5	3.5	4.0	5.0	2.7	2.3	2.3
SQa	5.3	5.3	2.7	3.5	2.6	4.0	5.0	2.7	2.3	1.7
Qd	5.3	5.3	3.7	4.0	4.0	3.5	5.0	2.7	2.3	3.0
POL	3.7	4.7	2.7	5.0	5.0	5.0	4.0	2.6	1.0	1.5
C3	3.5	2.7	3.5	2.7	2.7	2.7	2.6	3.5	3.5	3.5
C1	2.7	2.0	2.7	2.3	2.3	2.3	1.0	3.5	3.5	3.5
AR	2.7	2.0	2.0	2.3	1.7	3.0	1.5	3.5	3.5	2.6

Lennard-Jones parameter, σ (nm)

	PP1	PP5	PTN0	Qa	SQa	Qd	POL	C3	C1	AR
PP1	0.47	0.47	0.47	0.47	0.47	0.47	0.47	0.47	0.47	0.47
PP5	0.47	0.47	0.47	0.47	0.47	0.47	0.47	0.47	0.47	0.47
PTN0	0.47	0.47	0.32	0.47	0.43	0.47	0.47	0.47	0.47	0.43
Qa	0.47	0.47	0.47	0.47	0.47	0.47	0.47	0.47	0.47	0.47
SQa	0.47	0.47	0.43	0.47	0.43	0.47	0.47	0.47	0.47	0.43
Qd	0.47	0.47	0.47	0.47	0.47	0.47	0.47	0.47	0.47	0.47
POL	0.47	0.47	0.47	0.47	0.47	0.47	0.47	0.47	0.47	0.47
C3	0.47	0.47	0.47	0.47	0.47	0.47	0.47	0.47	0.47	0.47
C1	0.47	0.47	0.47	0.47	0.47	0.47	0.47	0.47	0.47	0.47
AR	0.47	0.47	0.43	0.47	0.43	0.47	0.47	0.47	0.47	0.43

Bonded interactions. Bonded parameters were defined in a way similar to our lab's CG model for the chitosan polysaccharide.[14] In brief, for each CG bond, angle or dihedral, atomistic references were generated by calculating bonds, angles, and dihedrals between the centres of mass of the atom groups mapping to each CG bead. Reference values and force constants of the CG bonded interaction terms were tuned until they matched their atomistic reference distributions (Figures S2, S3 and S4). All bonded interaction parameters are detailed in Tables S3, S4, and S5.

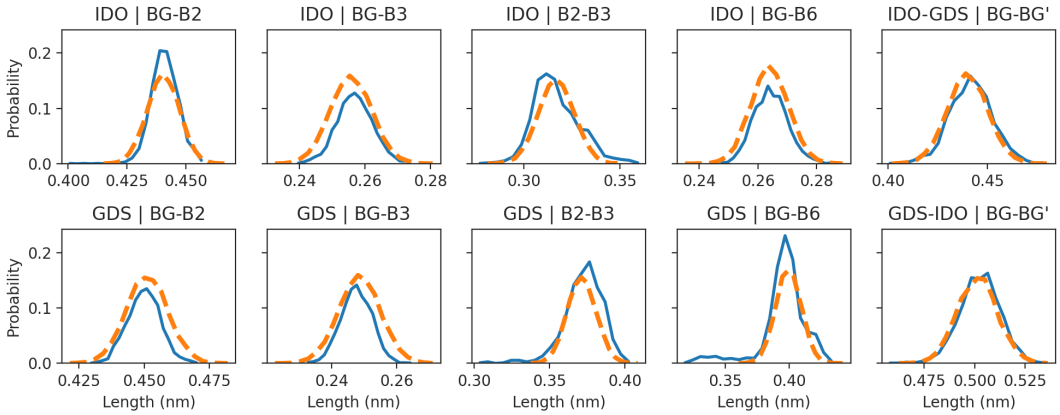

Figure S2: Distributions of CG bond lengths (dashed orange lines) and their atomistic references (solid blue lines).

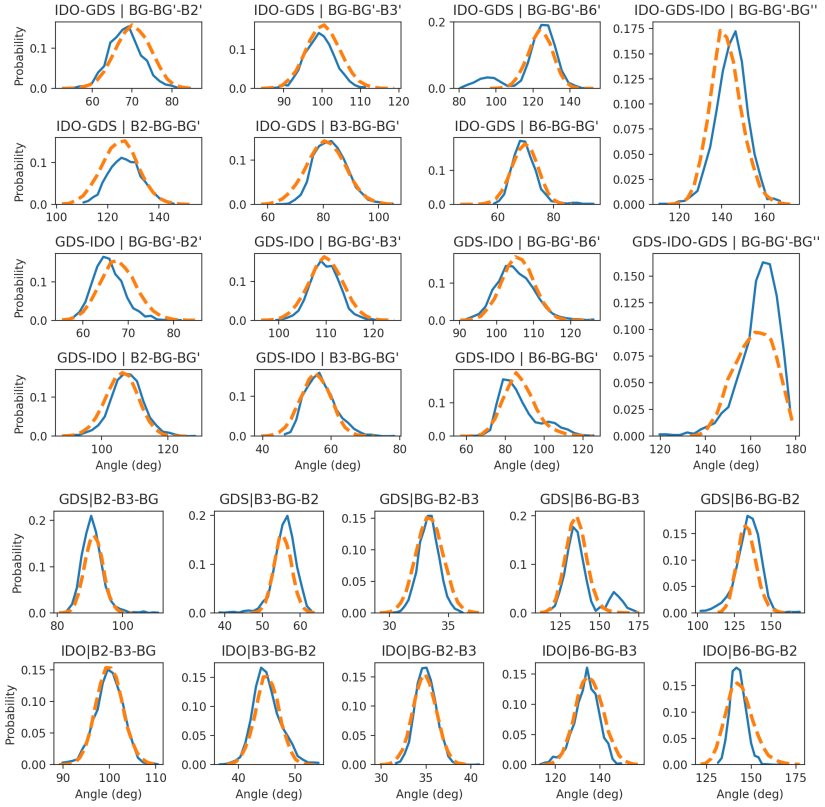

Figure S3: Distributions of CG angles (dashed orange lines) and their atomistic references (solid blue lines).

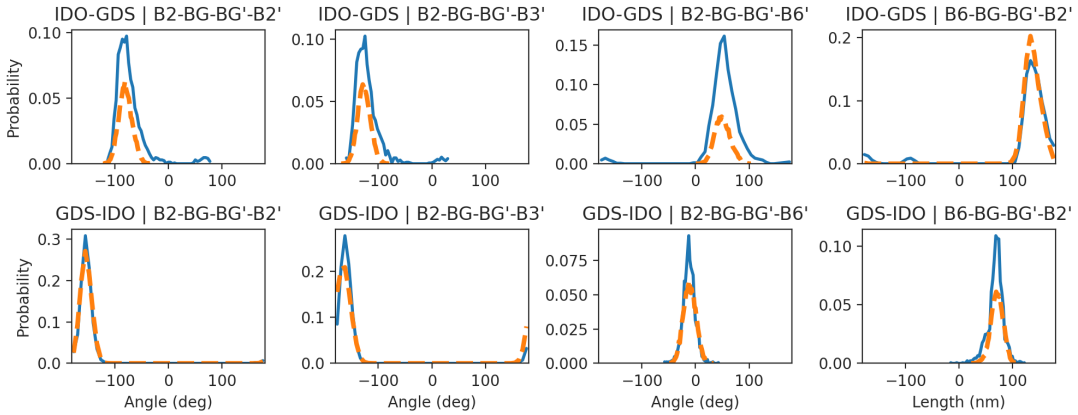

Figure S4: Distributions of CG dihedrals (dashed orange lines) and their atomistic references (solid blue lines).

Table S3: Parameters for bonds, represented by harmonic potentials of the form $V_{bond}(r) = \frac{1}{2}K_{bond}(r - r_0)^2$

Intra-residue bonds in IDO		
Bond type	r_0 (nm)	K_{bond} (kJ mol^{-1} nm^{-2})
BG-B2	0.441	60000.000
BG-B3	0.257	80000.000
B2-B3	0.320	25000.000
BG-B6	0.265	80000.000
BG-BGm	0.140	30000.000
BG-BGp	0.140	30000.000
B3-B3p	0.095	30000.000
B3-B3m	0.095	30000.000
Intra-residue bonds in GDS		
Bond type	r_0 (nm)	K_{bond} (kJ mol^{-1} nm^{-2})
BG-B2	0.450	40000.000
BG-B3	0.250	80000.000
B2-B3	0.375	25000.000
BG-B6	0.400	30000.000
BG-BGm	0.140	30000.000
BG-BGp	0.140	30000.000
B3-B3p	0.095	30000.000
B3-B3m	0.095	30000.000
IDO-GDS inter-residue bonds		
Bond type	r_0 (nm)	K_{bond} (kJ mol^{-1} nm^{-2})
BG-BG’	0.435	30000.000
GDS-IDO inter-residue bonds		
Bond type	r_0 (nm)	K_{bond} (kJ mol^{-1} nm^{-2})
BG-BG’	0.495	30000.000

Table S4: Parameters for angles, represented by cosine-based potentials of the form $V_{angle}(\theta) = \frac{1}{2}K_{angle}(cos(\theta) - cos(\theta_0))^2$

Intra-residue angles for IDO

	Reference angle, θ_0 (degrees)	K_{angle} (kJ mol^{-1})
B2-B3-BG	99.9	450.0
B3-BG-B2	45.1	300.0
B6-BG-B2	142.7	400.0
B6-BG-B3	140.0	350.0
BG-B2-B3	35.0	1000.0
BGm-BG-BGp	180.0	8.5
B3m-B3-B3p	180.0	3.0

Intra-residue angles for GDS

Angle type	θ_0 (degrees)	K_{angle} (kJ mol^{-1})
B2-B3-BG	90.8	450.0
B3-BG-B2	55.6	300.0
B6-BG-B2	155.0	250.0
B6-BG-B3	137.5	200.0
BG-B2-B3	33.3	1000.0
BGm-BG-BGp	180.0	35.0
B3m-B3-B3p	180.0	3.0

IDO-GDS inter-residue angles

Angle type	θ_0 (degrees)	K_{angle} (kJ mol^{-1})
BG-BG'-B2'	68.4	450.0
BG-BG'-B3'	99.3	450.0
BG-BG'-B6'	140.0	80.0
B2-BG-BG'	125.0	100.0
B3-BG-BG'	77.7	100.0
B6-BG-BG'	66.0	450.0

GDS-IDO inter-residue angles

Angle type	θ_0 (degrees)	K_{angle} (kJ mol^{-1})
B2-BG-BG'	107.6	300.0
B3-BG-BG'	56.9	300.0
B6-BG-BG'	77.0	80.0
BG-BG'-B2'	65.6	450.0
BG-BG'-B3'	109.7	450.0
BG-BG'-B6'	105.0	300.0

IDO-GDS-IDO inter-residue angles

Angle type	θ_0 (degrees)	K_{angle} (kJ mol^{-1})
BG-BG'-BG"	150.0	125.0

GDS-IDO-GDS inter-residue angles

Angle type	θ_0 (degrees)	K_{angle} (kJ mol^{-1})
BG-BG'-BG"	175.0	125.0

Table S5: Parameters for dihedrals, represented by periodic-type potentials of the form $V_{dihedral}(\phi) = K_{dihedral}(1 + cos(\phi - \phi_s))$

IDO-IDO-GDS-GDS inter-residue dihedrals

Dihedral type	ϕ_s (degrees)	$K_{dihedral}$ (kJ mol^{-1})
B2-BG-BG'-B2'	115	20.0
B2-BG-BG'-B3'	60	20.0
B2-BG-BG'-B6'	−105	15.0
B6-BG-BG'-B2'	−20	15.0

GDS-GDS-IDO-IDO inter-residue dihedrals

Dihedral type	ϕ_s (degrees)	$K_{dihedral}$ (kJ mol^{-1})
B2-BG-BG'-B2'	25	20.0
B2-BG-BG'-B3'	15	20.0
B2-BG-BG'-B6'	165	40.0
B6-BG-BG'-B2'	−114	40.0

1.2.1 CG Heparin Model Validation

The CG model was able to capture the characteristic torsional angles of both the glycosidic linkages, IDO-(1-4)-GDS and GDS-(1-4)-IDO. The final distributions for these characteristic torsional angles, other bonded interactions and dipole moments against the atomistic reference data are presented in Figure S5. We simulated CG heparin fragments of varying lengths and found that the CG model reproduced experimentally measured trends in radius of gyration [1] across degrees of polymerization ranging from 2 to 36 (Figure S6).

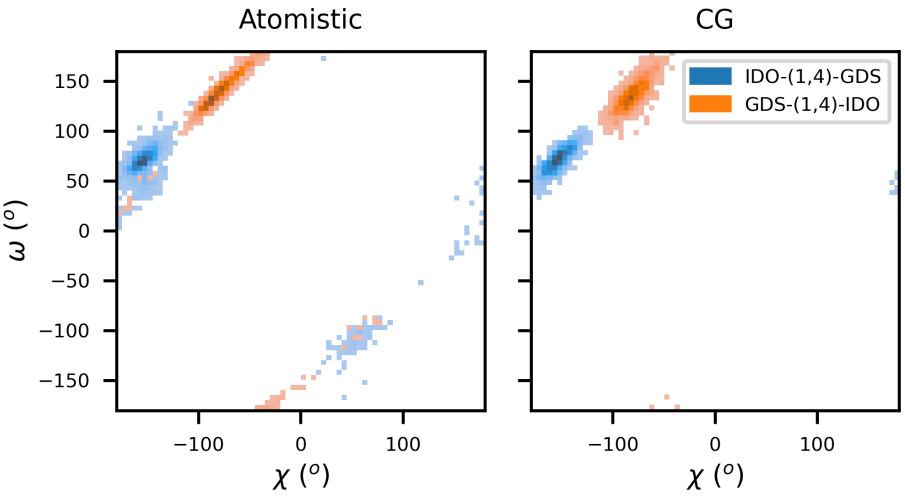

Figure S5: Comparison of characteristic torsion angles, χ:B6i-BGi-BGii-B6ii and ω:B3i-BGi-BGii-B3ii, spanning the GDS-(1,4)-IDO and IDO-(1,4)-GDS disaccharide linkages

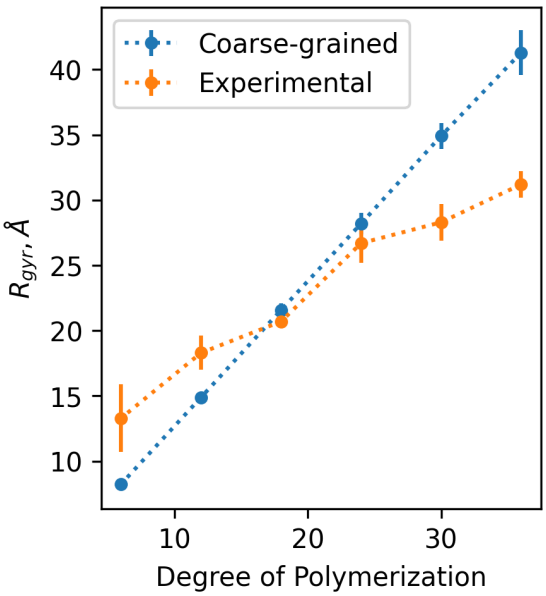

Figure S6: Radii of gyration of CG heparin fragments (blue trace) compared against experimental measurements (orange trace) from Khan et al. [1] at various degrees of polymerization

2 Supplementary Figures and Tables

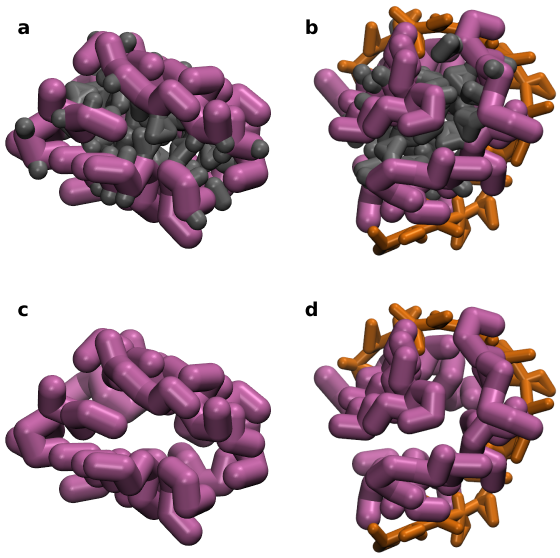

Figure S7: Representative snapshots of $A\beta_{16-22}$ aggregates with hydrophobic sidechains represented in grey (a and b), and hydrophobic sidechains hidden (c and d), thus showing the presence of characteristic hydrophobic cores. Aggregates formed in water are shown in a and c, alongside aggregates formed in the presence of a single dp18 heparin chain in b and d, at $N_{pep} = 16$. Heparin chains are represented in orange, and peptide backbones are represented in pink.

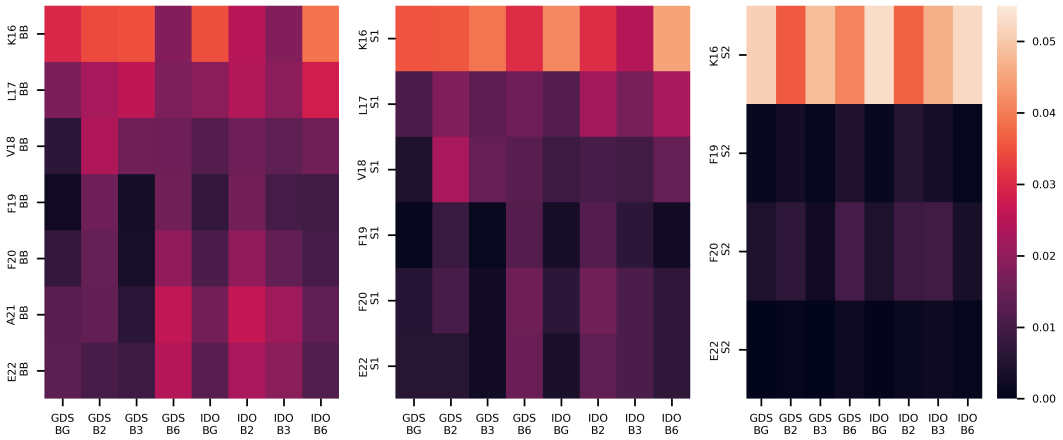

Figure S8: Contact maps between the various peptide beads (y-axis) and heparin beads (x-axis), for $A\beta_{16-22}$ aggregation with dp18 heparin at $N_{pep} = 16$. Contacts were counted every 1 ns, over the last 1000 ns of four independent replica simulations, and normalized by the number of peptides, number of heparin disaccharide units, and number of data points across all replicas.

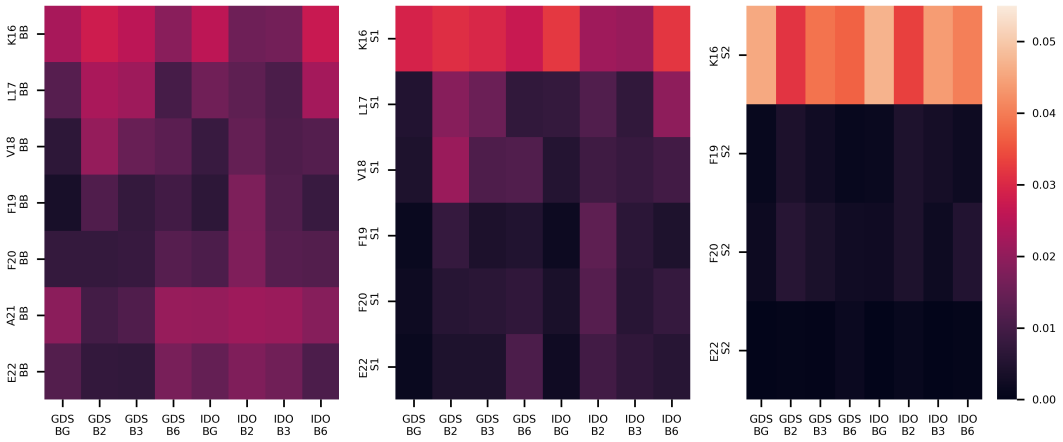

Figure S9: Contact maps between the various peptide beads (y-axis) and heparin beads (x-axis), for $A\beta_{16-22}$ aggregation with dp18 rigid heparin$_{200}$ at $N_{pep} = 16$. Contacts were counted every 1 ns, over the last 1000 ns of four independent replica simulations, and normalized by the number of peptides, number of heparin disaccharide units, and number of data points across all replicas.

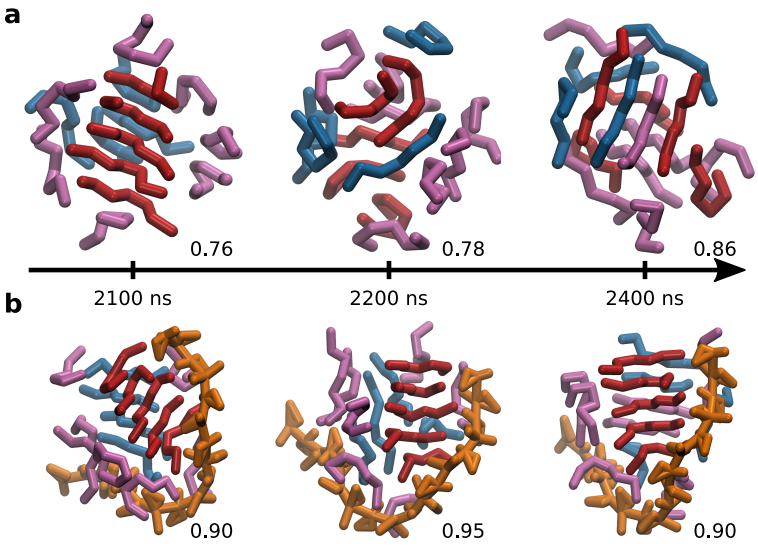

Figure S10: Mixing of peptides between beta-domains depicted by snapshots of $A\beta_{16-22}$ aggregation in water (a) and with dp18 heparin (b) annotated with their respective $\langle Q \rangle$ values at three time-points. Beta-domains at the initial time-point, 2100 ns, are coloured in red and blue, while all other peptides are coloured in pink, and heparin is coloured in orange. Peptides forming distinct beta-domains at the initial time-point, 2100 ns, are coloured in red and blue, while all other peptides are coloured in pink, and heparin is coloured in orange. Colourings are preserved from one time-point to the next.

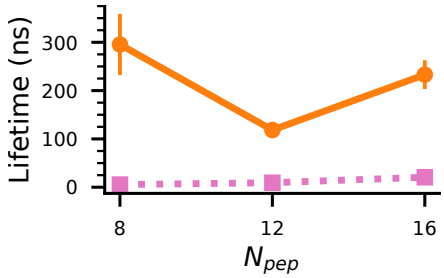

Figure S11: Mean lifetimes of beta-domains at different numbers of peptides, N_{pep}. Data for $A\beta_{16-22}$ aggregation in water and with dp18 heparin are traced by pink squares connected by dotted lines and orange circles connected by solid lines, respectively. Data were averaged over the last 1000 ns of four independent replica simulations, with error bars depicting ± 2 standard errors. Lifetimes were averaged by weighing lifetimes by themselves so that long-lived beta-domains are given more importance than very short-lived domains with near-zero lifetimes.

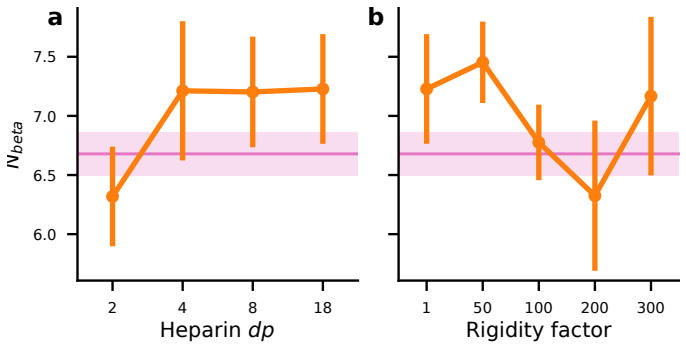

Figure S12: Average number of beta-strands at varying heparin *dp*'s (a) and varying heparin rigidities (c). Average numbers of beta strands, at $N_{pep} = 16$, at the test conditions are shown as orange circles against the baseline number for $N_{pep} = 16$ $A\beta_{16-22}$ peptides in water. Averages were calculated over the last 1000 ns of four independent replica simulations sampled at 1 ns intervals, with error bars and shaded regions depicting ±2 standard errors.

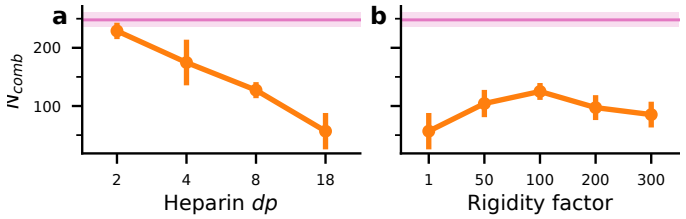

Figure S13: Average numbers of beta domain combinations, N_{comb}, at varying heparin *dp*'s (a) and varying heparin rigidities (c) at $N_{pep} = 16$. N_{comb} is related to the entropy of mixing by the expression $S^{mix} = k_B ln(N_{comb})$ where k_B is the Boltzmann constant. N_{comb} at the test conditions are shown as orange circles against the baseline number for $N_{pep} = 16$ $A\beta_{16-22}$ peptides in water. Averages were calculated over the last 1000 ns of four independent replica simulations sampled at 1 ns intervals, with error bars and shaded regions depicting ±2 standard errors.

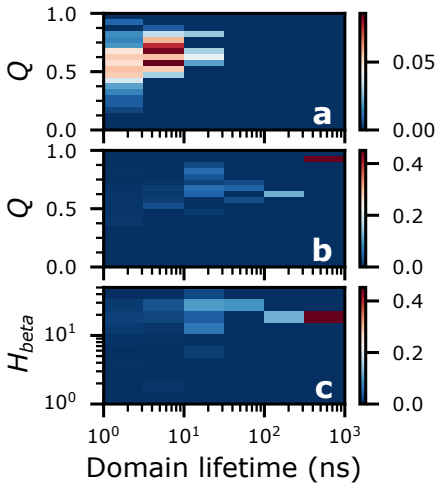

Figure S14: Probability distributions of beta-domains' Q against their lifetimes for $A\beta_{16-22}$ aggregation at $N_{pep} = 8$ in water (a) and with dp18 heparin (b). Probability distribution of heparin contacts per peptide, H_{beta}, and lifetimes of beta-domains for $A\beta_{16-22}$ at $N_{pep} = 8$ with dp18 heparin (c). Data were taken from the last 1 μs of four independent trials; error bars denote two standard errors (SE).

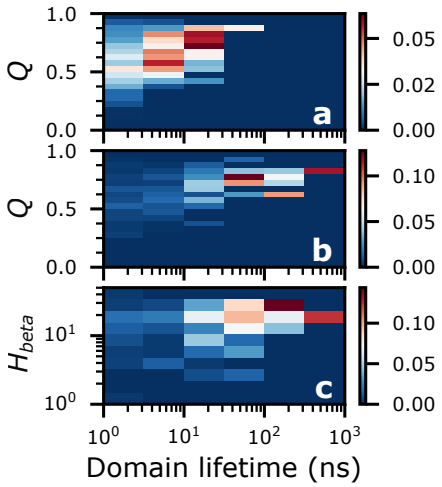

Figure S15: Probability distributions of beta-domains' Q against their lifetimes for $A\beta_{16-22}$ aggregation at $N_{pep} = 12$ in water (a) and with dp18 heparin (b). Probability distribution of heparin contacts per peptide, H_{beta}, and lifetimes of beta-domains for $A\beta_{16-22}$ at $N_{pep} = 12$ with dp18 heparin (c). Data were taken from the last 1 μs of four independent trials; error bars denote two standard errors (SE).

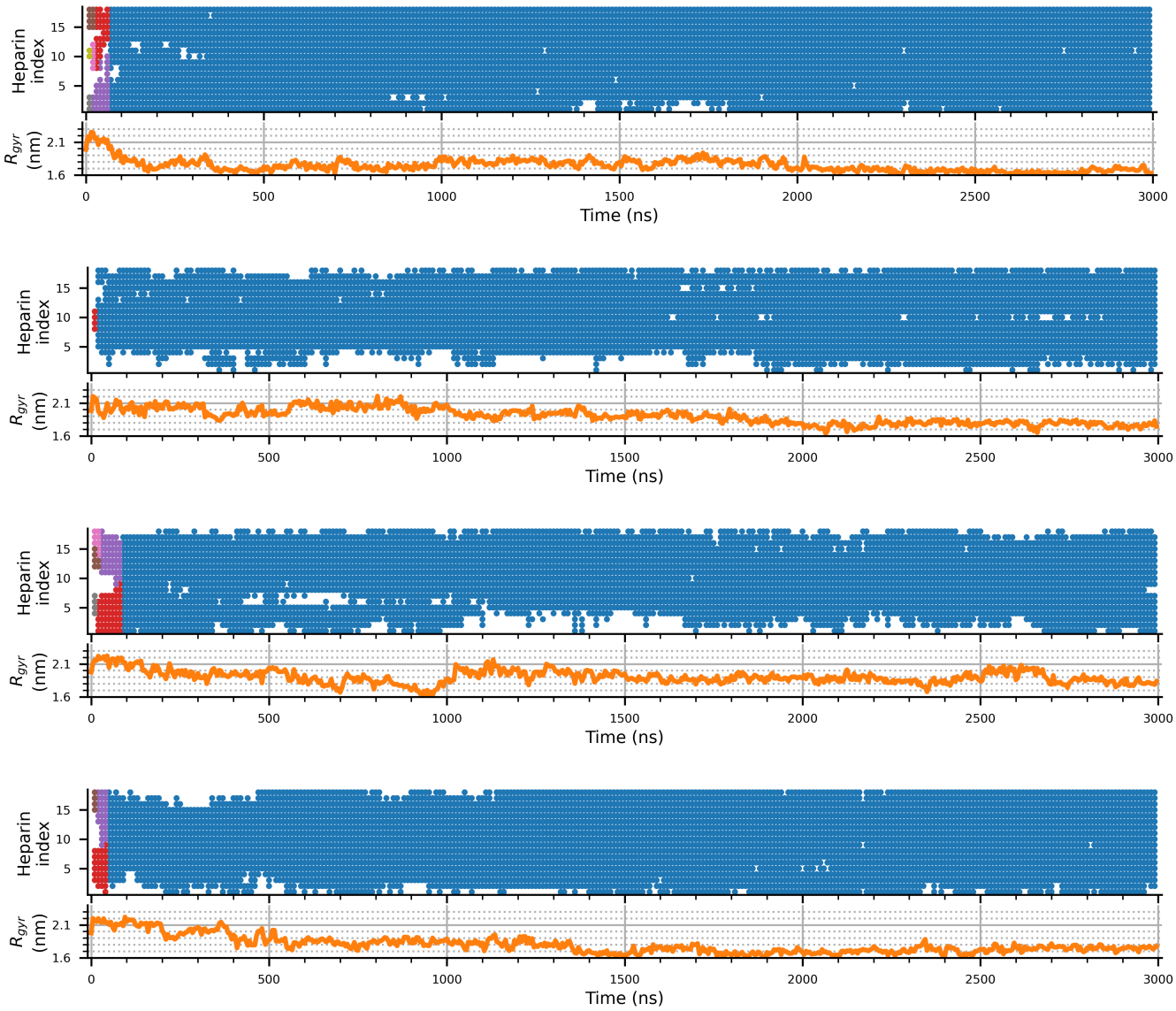

Figure S16: $A\beta_{16-22}$ **aggregation at** $N_{pep} = 16$ **with dp18 heparin.** Each row shows heparin residue indices bound by peptide aggregates (top) and radius of gyration of heparin molecules, R_{gyr} (bottom) as a function of time at one of four replica simulations. Heparin residue indices are marked by colours corresponding to distinct aggregates, distinguished by the set of their constituent peptide id's.

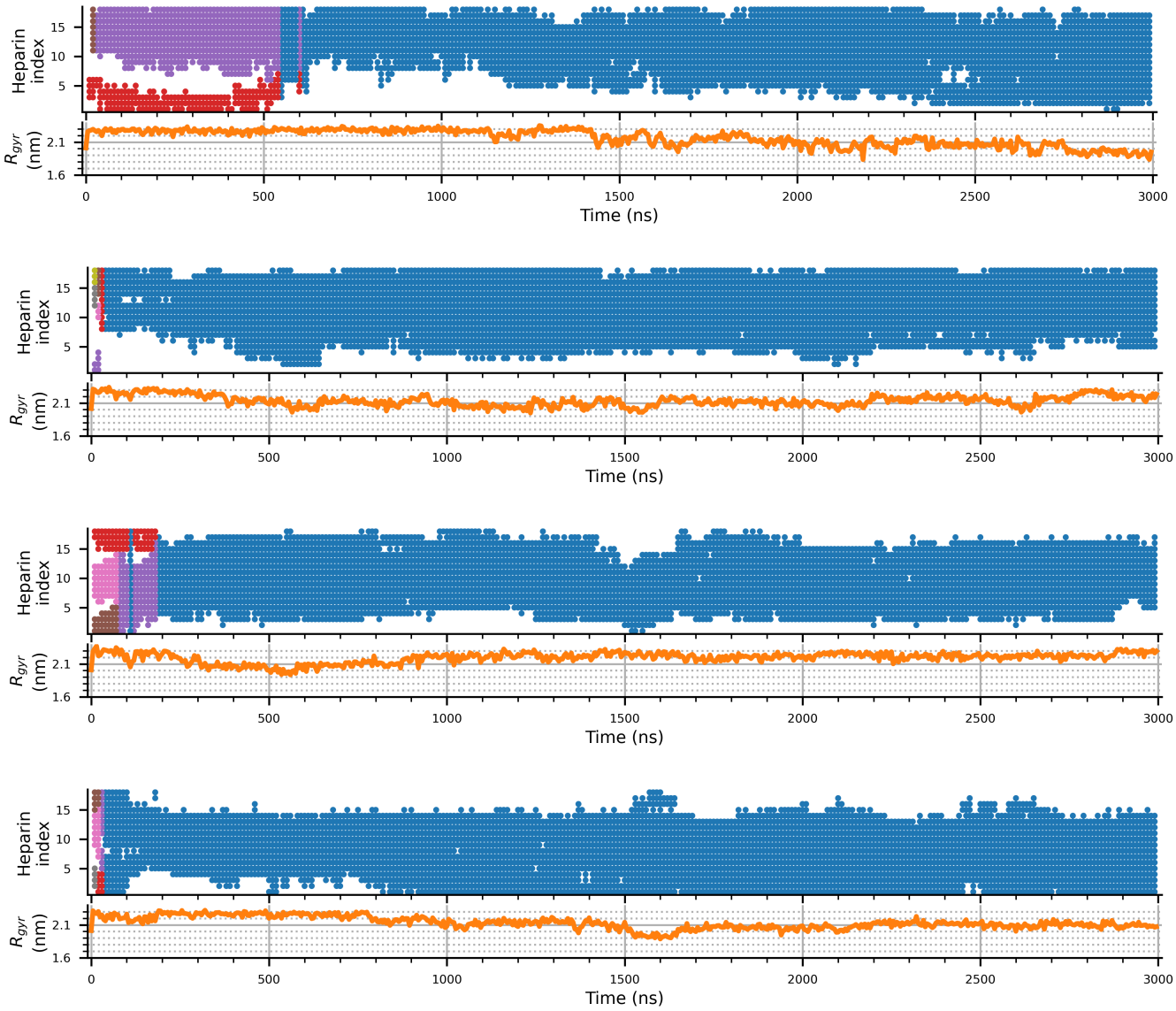

Figure S17: $A\beta_{16-22}$ **aggregation at** $N_{pep} = 16$ **with dp18 heparin**$_{50}$**.** Each row shows heparin residue indices bound by peptide aggregates (top) and radius of gyration of heparin molecules, R_{gyr} (bottom) as a function of time at one of four replica simulations. Heparin residue indices are marked by colours corresponding to distinct aggregates, distinguished by the set of their constituent peptide id's.

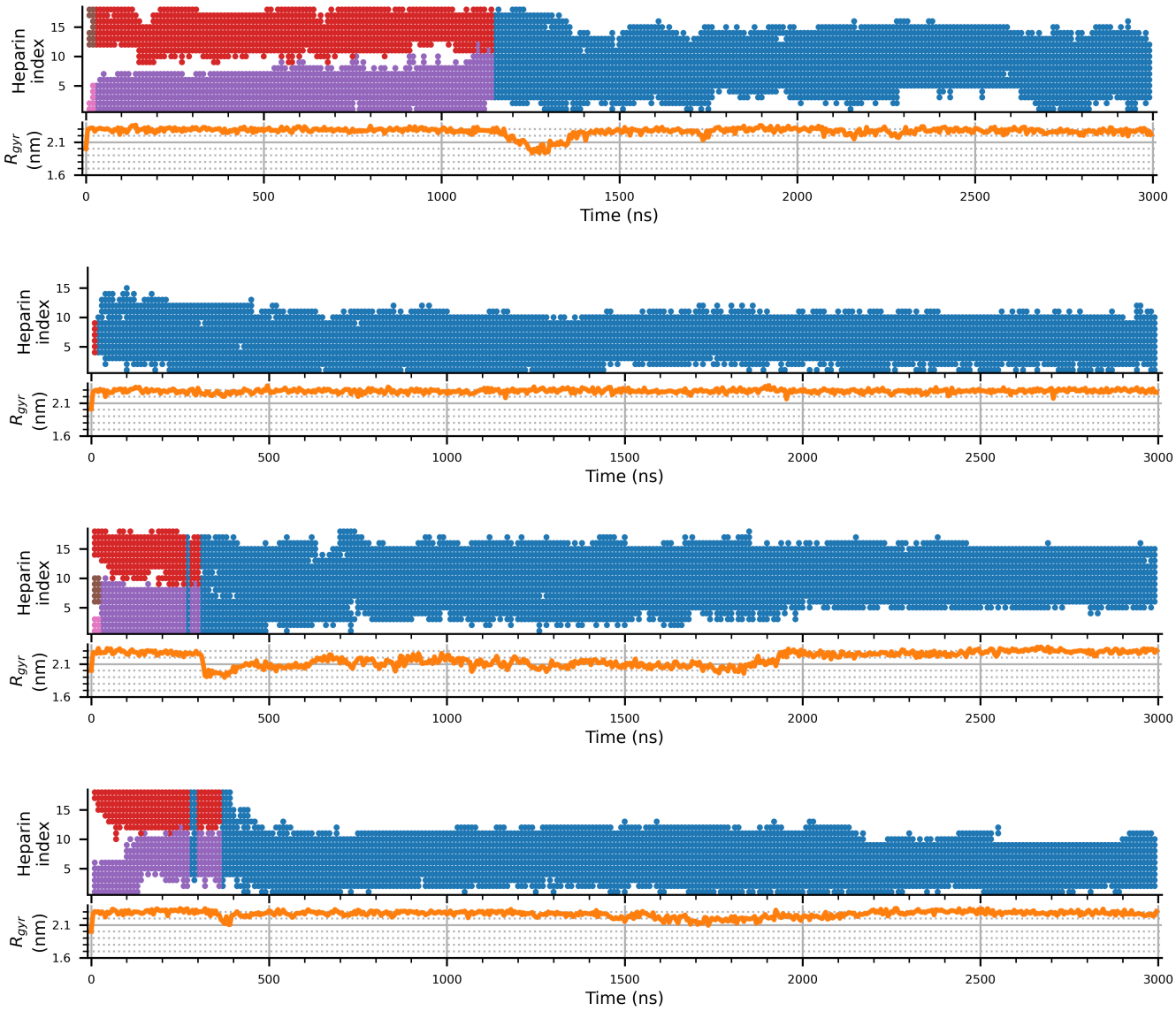

Figure S18: $A\beta_{16-22}$ **aggregation at** $N_{pep} = 16$ **with dp18 heparin**$_{100}$**.** Each row shows heparin residue indices bound by peptide aggregates (top) and radius of gyration of heparin molecules, R_{gyr} (bottom) as a function of time at one of four replica simulations. Heparin residue indices are marked by colours corresponding to distinct aggregates, distinguished by the set of their constituent peptide id's.

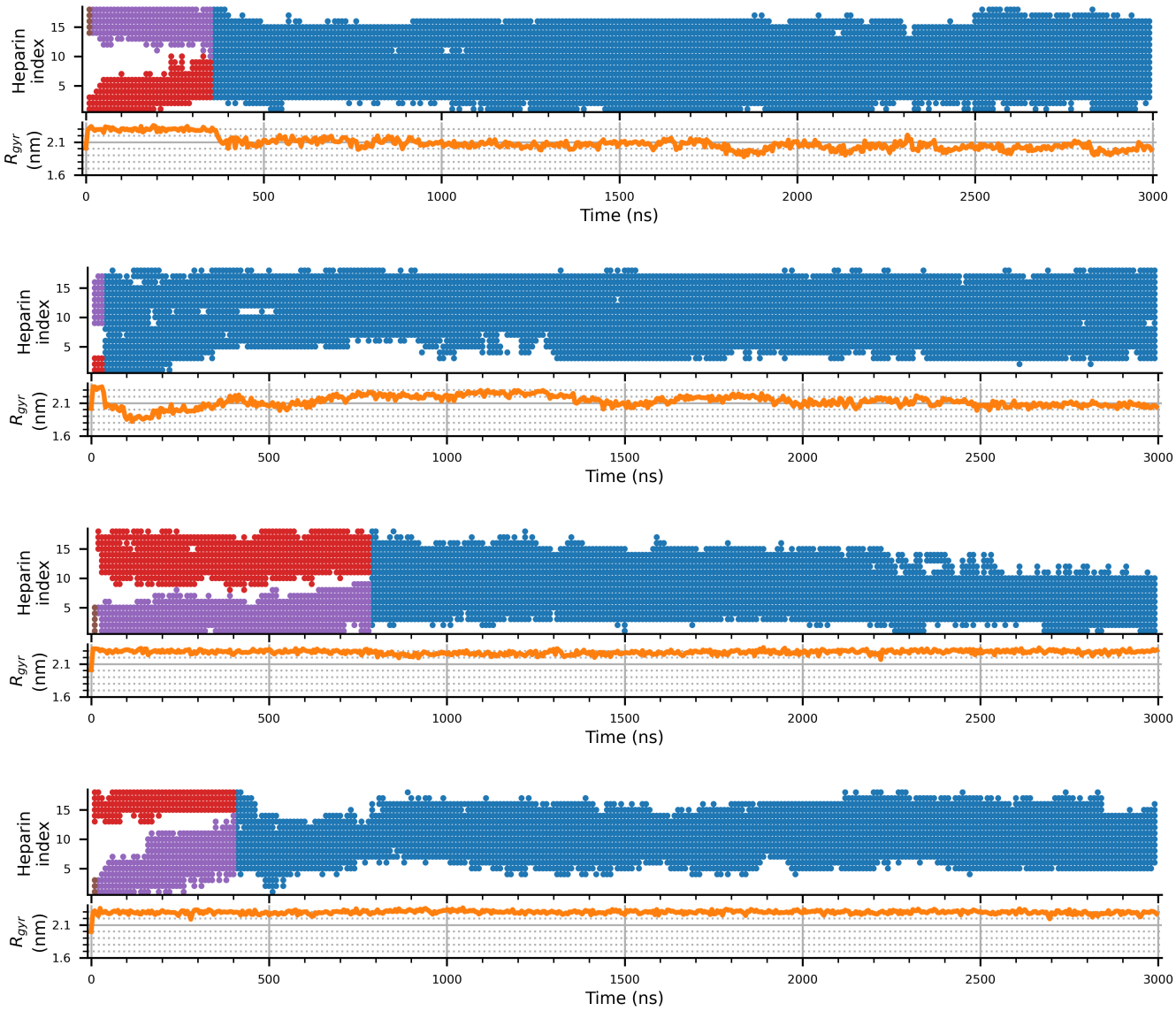

Figure S19: $A\beta_{16-22}$ **aggregation at** $N_{pep} = 16$ **with dp18 heparin**$_{200}$**.** Each row shows heparin residue indices bound by peptide aggregates (top) and radius of gyration of heparin molecules, R_{gyr} (bottom) as a function of time at one of four replica simulations. Heparin residue indices are marked by colours corresponding to distinct aggregates, distinguished by the set of their constituent peptide id's.

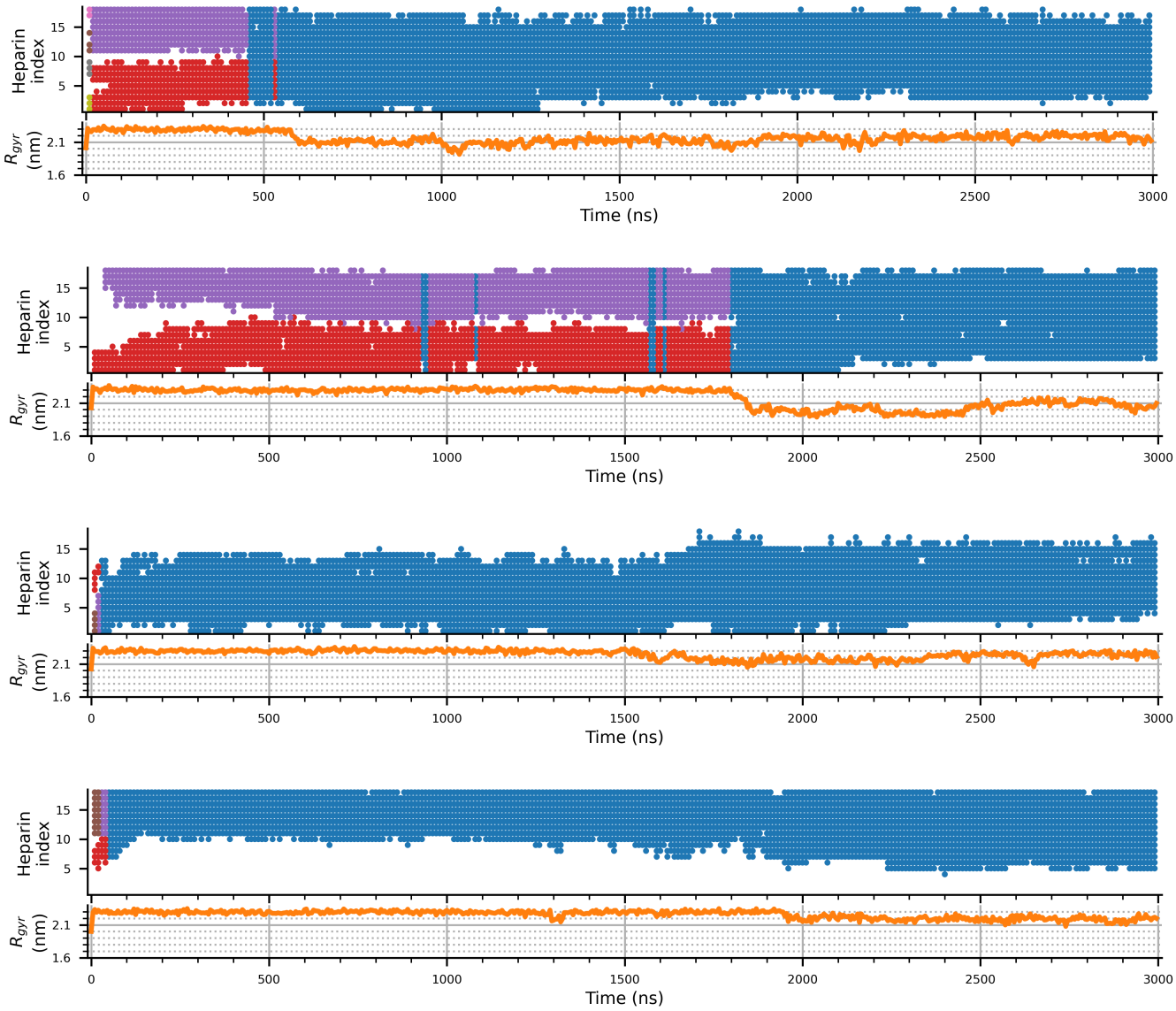

Figure S20: $A\beta_{16-22}$ **aggregation at** $N_{pep} = 16$ **with dp18 heparin**$_{300}$**.** Each row shows heparin residue indices bound by peptide aggregates (top) and radius of gyration of heparin molecules, R_{gyr} (bottom) as a function of time at one of four replica simulations. Heparin residue indices are marked by colours corresponding to distinct aggregates, distinguished by the set of their constituent peptide id's.

3 Supplementary Movie Captions

Movie S1.

Movie showing the aggregation of $A\beta_{16-22}$ peptides (translucent pink volumes) with $dp18$ heparin$_1$ (orange strand).

Movie S2.

Movie showing the aggregation of $A\beta_{16-22}$ peptides (translucent pink volumes) with $dp18$ heparin$_{200}$ (orange strand).

References

[1] S. Khan, J. Gor, B. Mulloy and S. J. Perkins, *J. Mol. Biol.*, 2010, **395**, 504–521.

[2] O. Guvench, S. S. Mallajosyula, E. P. Raman, E. Hatcher, K. Vanommeslaeghe, T. J. Foster, F. W. I. Jamison and A. D. J. MacKerell, *J. Chem. Theory Comput.*, 2011, **7**, 3162–3180.

[3] S.-J. Park, J. Lee, Y. Qi, N. R. Kern, H. S. Lee, S. Jo, I. Joung, K. Joo, J. Lee and W. Im, *Glycobiology*, 2019, **29**, 320–331.

[4] S. Jo, T. Kim, V. G. Iyer and W. Im, *J. Comput. Chem.*, 2008, **29**, 1859–1865.

[5] J. Lee, X. Cheng, J. M. Swails, M. S. Yeom, P. K. Eastman, J. A. Lemkul, S. Wei, J. Buckner, J. C. Jeong, Y. Qi, S. Jo, V. S. Pande, D. A. Case, C. L. I. Brooks, A. D. J. MacKerell, J. B. Klauda and W. Im, *J. Chem. Theory Comput.*, 2016, **12**, 405–413.

[6] B. R. Brooks, C. L. Brooks III, A. D. Mackerell Jr., L. Nilsson, R. J. Petrella, B. Roux, Y. Won, G. Archontis, C. Bartels, S. Boresch, A. Caflisch, L. Caves, Q. Cui, A. R. Dinner, M. Feig, S. Fischer, J. Gao, M. Hodoscek, W. Im, K. Kuczera, T. Lazaridis, J. Ma, V. Ovchinnikov, E. Paci, R. W. Pastor, C. B. Post, J. Z. Pu, M. Schaefer, B. Tidor, R. M. Venable, H. L. Woodcock, X. Wu, W. Yang, D. M. York and M. Karplus, *J. Comput. Chem.*, 2009, **30**, 1545–1614.

[7] B. Hess, H. Bekker, H. J. C. Berendsen and J. G. E. M. Fraaije, *J. Comput. Chem.*, 1997, **18**, 1463–1472.

[8] M. Parrinello and A. Rahman, *J. Appl. Phys.*, 1981, **52**, 7182–7190.

[9] D. J. Evans and B. L. Holian, *J. Chem. Phys.*, 1985, **83**, 4069–4074.

[10] T. Darden, D. York and L. Pedersen, *J. Chem. Phys.*, 1993, **98**, 10089–10092.

[11] J. J. Uusitalo, H. I. Ingólfsson, P. Akhshi, D. P. Tieleman and S. J. Marrink, *J. Chem. Theory Comput.*, 2015, **11**, 3932–3945.

[12] S. O. Yesylevskyy, L. V. Schäfer, D. Sengupta and S. J. Marrink, *PLoS Comput. Biol.*, 2010, **6**, e1000810.

[13] A. Sahoo, P.-Y. Lee and S. Matysiak, *J. Chem. Theory Comput.*, 2022, **18**, 5046–5055.

[14] H. Xu and S. Matysiak, *Chem. Commun.*, 2017, **53**, 7373–7376.